Gravitationally Lensed Image Simulations for the Study of Substructure in Galaxy Clusters

by

Molly S. Peeples

Submitted to the Department of Physics
in partial fulfillment of the requirements for the degree of

Bachelor of Science in Physics

at the

MASSACHUSETTS INSTITUTE OF TECHNOLOGY

May 2005 [June 2005]

Author .....
Department of Physics
May 6, 2005

Certified by .....
Professor Paul L. Schechter
William A. M. Burden Professor of Astrophysics
Thesis Supervisor

Certified by .....
Dr. Richard Massey
Caltech Department of Astronomy
Thesis Supervisor

Accepted by .....
Professor David E. Prichard
Senior Thesis Coordinator, Department of Physics

Gravitationally Lensed Image Simulations for the Study of Substructure in Galaxy Clusters

by

Molly S. Peeples

Submitted to the Department of Physics
on May 6, 2005, in partial fulfillment of the
requirements for the degree of
Bachelor of Science in Physics

Abstract

As gravitational lensing is susceptible to all gravitating matter—both baryonic and dark—it provides a potentially clean way to study the mass distribution of galaxy clusters. We are particularly interested in the substructure of dark matter in galaxy clusters as it signals constraints on various cosmological parameters as well as cluster evolution. Gravitationally lensed image simulations are needed in order to determine just how much can be learned from current mass reconstruction methods. We present here a comprehensive procedure for generating such a set of simulated images using shapelets (Massey et al. (2005)). These images use a catalog of galaxies from the Hubble Space Telescope data taken as part of the Cosmos Evolution Survey (COSMOS). The background galaxies are then lensed by a $10^{15} M_{\odot}$ galaxy cluster set at a redshift of $z = 0.4$. Noise and a point spread function (PSF) can also be added to the images; we chose to emulate the set of COSMOS pointings from the Subaru Telescope. As the shapelets simulation software allows complete freedom over all background galaxy, noise, and PSF parameters, the methods presented here have the potential to be used to not only verify that existing mass reconstruction algorithms work, but also to help optimize specifications on future telescopes. We also present a preliminary strong lensing analysis of two noise- and PSF-free simulated images according to the algorithm presented in Diego et al. (2005). We found that while this procedure was able to accurately reproduce the surface mass density profile for radii greater than that of the outermost arcs used in the analysis, it failed in unexpected ways for the inner radii.

Thesis Supervisor: Professor Paul L. Schechter
Title: William A. M. Burden Professor of Astrophysics

Thesis Supervisor: Dr. Richard Massey
Title: Postdoctoral Research Fellow, Caltech Department of Astronomy

Acknowledgments

This thesis would not have happened at all if it hadn't been for the copious amounts of help from my two advisors, Paul Schechter and Richard Massey. The term "advisor" here is unsatisfactory; an advisor is someone who merely gives advice, which can then be either adhered to or ignored. *My* advisors have been more than that; they are teachers.

I first started working with Paul Schechter the summer of 2003. I knew from the outset that this was a lucky thing, as he was the first professor at MIT I had encountered whose initial assessment of my potential to succeed in physics was not based on my grades in physics classes. Over the last two years, I have learned much about how to tackle a given problem—and not just from the constant deluge of Schechter-isms, e.g., less is more; Zipf's Law; approximate ruthlessly... It is clear to me that my approach to physics will always be strongly influenced by all of his pedagogy I've unconsciously picked up through the many hours spent at his chalkboard and the many back-and-forth emails.

Richard Massey was initially one of my co-advisors for my summer research fellowship at Caltech during the summer of 2004. Richard's enthusiasm for the elegance and potential of shapelets to model astrophysical objects is quite contagious. Even long-distance, dicsussions with him have always helped me to see things in such a light that I am able to understand them better. It was also from him that I learned how to code (and debug) *well*—as it turns out, readable code is much more useful and effective than messy, uncommented code.

Thank you to Jose Diego for the numerous hours dedicated to helping me get my raytracing program to work, as well as all of the strong lensing analysis... and the very-last-minute analysis, re-analysis, question answering and more question answering.

I am very grateful for being able to work at Caltech on such an interesting project with such interesting people. I was technically working under Richard Ellis, who has always proved to be an outstanding source of excellent advice—as well as funding, both of which I am very appreciative. I would not have been able to get to Caltech

if it hadn't been for Jason Rhodes, who has an good knack for getting these kinds of organizational things taken care of. I gained much from Jason's excited teachings about cosmic shear measurements and PSF causes (excited? PSF? yes, indeedy), not to mention his unique take on pretty much any topic. I was also lucky enough to be working alongside Will High, who got his B.S. from Berkeley this past December. Much thanks to Will for being able to work comfortably in the same office as someone who can't sit still for an entire half hour. My current take on physics, both science and politics-wise, is greatly influenced by our many discussions, most of which happened when we should have been working. Thanks also to Nick Scoville and Alexandre Refregier for their occasional yet quite helpful suggestions, advice, and input.

Many muchly-filled thanks to Nick Fotopoulos for all of the useful conversations, rant sessions, physics discussions, stalkings, good ideas, paper readings, image oglings, esteem boosts, and stress reliefs over the last two years. I would also like to thank my friends, especially Katherine Lai, Yuran Lu, Oliver Kosut,  , and the rest of the crowd on `-c molly`, for their constant moral support. Finally, I thank my family for at least pretending to understand why they haven't really heard from me in the last month.

This thesis was brought to you by the letter "caffeine," which was brought to me by the guys at Toscanini's and the ladies at the Lobby 7 Coffee Shop.

Preface

This research was started during the summer of 2004 when I had a summer research fellowship at Caltech under Richard Ellis. Though the fellowship had been mostly set up through Jason Rhodes, I wound up working primarily with Richard Massey to create a set of image simulations for the calibration of cosmic shear measurements. It was in this context that I did the work behind the catalogs discussed in §2.1.1 and the PSF and noise parameters discussed in §2.3. The basic shapelets simulation software was written by Richard Massey and Alexandre Refregier. Aside from finding various bugs in the code, I manipulated it in order to incorporate the Subaru COSMOS emulation. After returning to MIT, I worked with my advisors, Paul Schechter (with whom I had worked on an unrelated project in gravitational lensing the previous year) and Richard Massey, to settle on an appropriate thesis topic. I then returned to Caltech for three weeks during January 2005, primarily funded by Richard Ellis, to incorporate the use of different redshift bins as well as a generic raytracing program into the shapelets image simulation software.

Back at MIT, I wrote the raytracing program discussed in §2.2 with help from Paul Schechter and Jose Diego. The idea to use Fourier space to speed up the raytracing program, as well as much help in the implementation thereof, came from Jose Diego. It was Paul Schechter's idea to use α-matching at the array edges to decrease the associated errors. The original lensing cluster used came to me from Havard Sandvik via Jose Diego. The reconstructed clusters presented in Chapter 3 were created by Jose Diego using the algorithm discussed in the same chapter.

All of the code used here was written in IDL. All of the programming and script-running that I did was done on computers belonging to the COSMOS division of the

Astronomy department at Caltech.

Figure 1-1 is courtesy of Richard Massey. Figures 3-2 and 3-1 are thanks to Jose Diego.

Contents

List of Figures

Chapter 1

Background and Motivation

Gravitational lensing has increasingly become a popular way to study the gravitational potentials, and therefore mass distributions, of galaxy clusters. Insights into the substructure of galaxy clusters can reveal much about the nature of dark matter, the dynamics of galaxies in large gravitational fields, and the evolution of clusters. It is unknown just how much can currently be learned about the substructure of galaxy clusters by studying gravitationally lensed images. It is furthermore unknown whether the limitations on our current abilities to reconstruct such mass profiles are due to the quality of data available, or the current mass reconstruction algorithms, or both. Gravitationally lensed image simulations are therefore needed to answer the question of how good data must be in order for current mass reconstruction methods to accurately reconstruct the mass profiles of typical galaxy clusters. We present here such a set of image simulations, along with a preliminary strong lensing analysis of said images.

In this chapter, we give an overview of galaxy clusters and why they are interesting in §1.1. We present a summary of the theory of gravitational lensing in §1.2, and a more detailed motivation of the need for simulated images in §1.3. In Chapter 2, we explain how our image simulations were created. A preliminary strong lensing analysis of these images is given in Chapter 3. We conclude in Chapter 4 with a discussion on how these simulations could be made more realistic, and how a more accurate cluster mass distribution could be gleaned from them.

1.1 Galaxy Clusters

In general, galaxies are not free objects; they are gravitationally bound to, or at least gravitationally interacting with, some nearby collection of other galaxies. The sizes of these structures fall along a continuous spectrum, ranging from small groups of only a few bright galaxies to massive clusters. "Rich" galaxy clusters have on the order of several hundred galaxies with a velocity dispersion of roughly 1000km/s, confined to a region of radius on the order of a 1–2 Mpc, with a total mass of 10^{15} $M_{\odot}$. Because galaxy clusters are the most massive objects in the universe, their number density is highly susceptible to the small initial fluctuations of the primordial universe; constraints on the amplitudes and extents of these fluctuations would greatly constrain Ω_M. Thus, we would like to have a good handle on the number density and mass of galaxy clusters. It has long been known from the study of galactic radial velocity curves that not all of the mass in a single galaxy can be attributed to luminous matter. The same has been found to be true for galaxy clusters: there must be a large amount of "dark" matter in clusters that does not couple with light; this discrepancy is expressed in terms of a mass-to-light ratio. The cold dark matter (CDM) model of the character of dark matter has emerged recently as a promising and well-constrained description of the nature of dark matter. One of the major contributions to CDM's success has been the observations of Wilkinson Microwave Anisotropy Probe, which imply that the dark matter must have been cold enough in the past to allow for complex structures—such as stars, galaxies, and clusters—to form in the universe.[Spergel et al.(2003)] A main prediction of the CDM theory is that dark matter clusters in the same way regardless of scale; that is, that from the richest clusters all the way down to dwarf galaxies, we expect for the dark matter density profile to fall off like $\rho \propto r^{-\beta}$ up to some scale-based radius, and then to fall of like $\rho \propto r^{-3}$. The value of β is still up for debate.[Navarro, Frenk, & White (1997)]

Not as much as would be liked is currently well understood about the evolution of galaxy clusters. They are believed to not yet be in thermal equilibrium; their galaxies still interact at a local level. As a cluster evolves, its galaxies—especially ones towards

the center—experience a much stronger gravitational field than galaxies in small groups. It is believed that due to the presence of large local gravitational fields and the fact that the galaxies are still crashing into one another, the dark matter associated with the individual galaxies is "stripped" off, becoming part of the smooth background dark matter of the cluster itself.[Natajaran et al. (2002), Roediger et al. (2005)] One way to gain insight and put constraints on this theory and ones like it is to examine the substructure of dark matter in clusters. That is, we would like to examine the question of what percentage of dark matter in a cluster is bound to individual galaxies as opposed to being continuously distributed.

In §1.1.1, we briefly outline what *is* known about galaxy clusters, as well as why this information is not yet sufficient enough to thoroughly study dark matter substructure. We summarize the current ways in which clusters are observed in §1.1.2, concluding with an explanation of why we believe gravitational lensing to be the most promising way to analyze the substructure of dark matter in galaxy clusters.

1.1.1 Current Numbers, Estimates, and Theories

The first catalog of rich galaxy clusters, the Abell clusters, show a density on the order of $10^{-5}h^3\text{Mpc}^{-3}$. Clusters are not in thermal equilibrium; there has only been time for most of the galaxies to make only two or three revolutions around the center of the cluster. This means that galaxies within the cluster are still interacting with one another—mergers are relatively common. The fact that cluster galaxies are still interacting locally is yet another reason why trying to study the gravitational potentials of clusters based on velocity dispersions of the individual galaxies is highly susceptible to line-of-sight biases.[Binney & Tremaine]

One conceivable way of studying the substructure of galaxy clusters is to compare the average mass per galaxy, total cluster mass, and total number of galaxies. While for a given cluster, each of these quantities can be roughly determined, these three parameters have not yet been constrained well enough for a given cluster to be able to answer simple questions about cluster substructure.

Typical galaxies in the larger clusters are elliptical, which are redder and older

than spiral galaxies such as the Milky Way, which are in turn more commonly found in small groups. It is reasonable to assume that the typical galaxy masses in these clusters are not representative of all galaxy masses.

It is currently not agreed upon how quickly the dark matter profiles of clusters fall off towards the cluster center. For profiles that follow a density fall off like $\rho \propto r^{-3}$ within a scale-based radius, there has been evidence for profiles with β anywhere from 0 (constant inner densities) to 1 (as with a singular isothermal sphere). There is little evidence for steeper inner profiles. [de Blok & Bosma (2002), de Blok et al. (2001), Simon et al. (2003), Swaters et al. (2003)]

1.1.2 Observational Techniques

Observationally, learning about cluster evolution translates to observing as many galaxy clusters of different sizes and redshifts as possible—or a carefully selected representative sample. The most obvious way to search for galaxy clusters is to search for large collections of galaxies within a certain diameter at approximately the same distance. This is exactly what George Abell did in the 1950's; clusters in his catalog of over 2000 are still being studied. The Abell clusters were selected for compactness and "richness"—at least 50 galaxies in the potential cluster had to be no more than two magnitudes dimmer than the third brightest object, and contained within a circle of radius $1.5h^{-1}$Mpc. The main problem with using this technique to study clusters is that we are not interested in *light*; we are interested in *mass*. Even if we were able to study the mass profiles of clusters selected in this manner, clusters bright in the optical bands do not necessarily have representative mass distributions.

Many clusters are known to be strong X-ray sources. This radiation is due to bremsstrahlung in the central regions of the cluster, where highly energized ions in hot interacting gasses emit radiation to conserve energy as they quickly decelerate. However, studies of galaxy clusters based on X-ray emission is also subject to similar problems as those selected optically. People have also proposed studying the mass distributions of clusters via the Sunyaev-Zeldovich effect, which is essentially Compton scattering of photons from the cosmic microwave background by electrons in galaxy

clusters. While this would in fact be a way to study the *baryonic* mass distribution of a cluster, it is still partial to the mass that couples with light—i.e., not all of the mass that interests us.

As discussed in the next section, through gravitational lensing, one is able to study the way paths of light from background sources are distorted by the gravitational potential of an intervening cluster. Because the gravitational potential is subject to *all* gravitating matter, this is the only way we are able to directly detect the effects and distribution of dark matter.

1.2 Gravitational Lensing

The study of galaxy clusters via gravitational lensing is one of analyzing how the gravitational potentials of a given galaxy cluster distort the light from background galaxies. A central lens causes round, compact background objects to appear squashed along the direction towards the lens center and stretched along the tangential direction. Because the relation between a given gravitational potential and the variations in light paths is precise, one can hope to reconstruct the lensing potential—and thus mass distribution—by studying the perceived distortions of background objects.

Here we present the relevant basics of gravitational lensing, as well as offering the motivation behind applying this elegant field to the study of galaxy clusters. For the sake of the following, mostly qualitative, discussion in this paper, all that is needed is in §1.2.1. The necessary mathematical foundation for understanding the specific subtleties in the raytracing algorithm, presented in §2.2, and the strong lensing analysis presented in 3.1 is given in §1.2.2.

1.2.1 Overview

Gravitational lensing is exactly what it sounds like: because light will always travel along a path of extremal action, a gravitational potential acts as a "lens," causing paths of light crossing the potential to not be straight lines. In the sense of normal optics, gravitational lenses are generally rather shoddy lenses because background ob-

jects are practically never "focussed," that is, rays emanating from the same point do not in general converge at the same point. However, because the way in which a path of light is altered by a gravitational lens is a direct and understandable consequence of the geometry of the lens, it is possible to study the image distortions in order to learn about the lensing gravitational potential.

In the strong lensing regime, multiply-imaged sources and large arcs are common. For a non-symmetric lens such as a galaxy cluster, the source locations subject to strong lensing are generally close to being immediately behind the most compact regions of the lens. Because of this, the distortions of strongly lensed objects contain information about the substructure of the cluster. One other other hand, in the weak lensing limit, the path of light is affected by much more by the entire cluster. By studying these objects, we can theoretically learn about the large-scale structure of the cluster, i.e., the overall mass profile and total cluster mass.

1.2.2 Mathematical Dealings

The geometry associated with light passing through a large, three dimensional object is fairly complicated. It is usually reasonable to approximate the mass distribution as a "thin screen." By projecting all of the mass onto a single plane at a single redshift, the problem of calculating the subtle curves followed by a single ray of light is reduced to calculating one deflection angle $\vec{\alpha}$, as shown in Figure 1-1. Light from a distance D_S and at a position on the source plane $\vec{\beta}$ is deflected by an angle $\hat{\vec{\alpha}}$ when it hits the lens plane. When the ray reaches the observer, its apparent source position is perceived to be $\vec{\theta}$. These are angular diameter distances; the formalism used here and in the code described in Chapter 2 is as explained in [Hogg (1999)]. The distance from the observer to the lens is given by D_L, from the observer to the source by D_S, and between the lens and the source by D_{LS}.

One important concept to note here is that a potentially complex problem with its roots in general relativity has been reduced to a fairly simple geometry problem. This geometry depends only on various angles, which in turn depend only on distances between the lens, the source, and the observer and the surface mass density of the

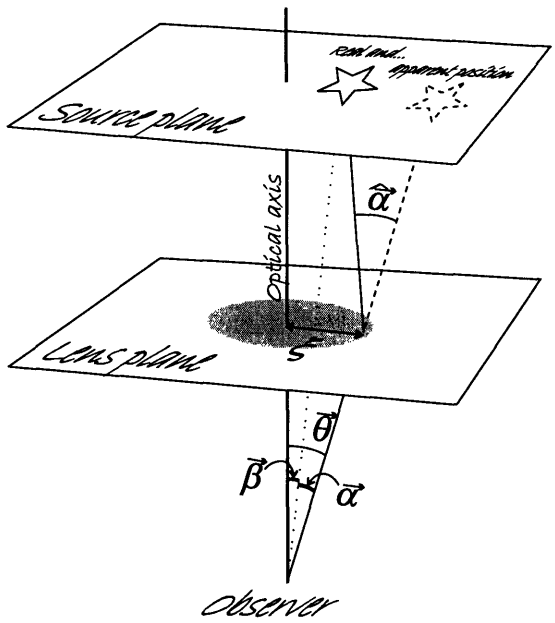

Figure 1-1: Light from the source plane is deflected by an angle $\hat{\vec{\alpha}}$ at the lens plane. The apparent position at the source plane is given by $\vec{\theta}$, the apparent deflection by $\vec{\alpha}$, and the real source position by $\vec{\beta}$. The physical distance $\vec{\theta}$ subtends in the lens plane is given by ζ.

lens sheet. As one can tell by examining Figure 1-1, the relation between these angles is

$$\vec{\beta} = \vec{\theta} - \vec{\alpha}(\vec{\theta}). \tag{1.1}$$

Equation (1.1) is known as the lens equation, and it is the main workhorse behind any raytracing algorithm, such as the one outlined in §2.2. Here, all angles are as measured by the observer: $\vec{\theta}$ is the location of the image and the only measurable in the equation, $\vec{\beta}$ gives the (unknown) location of the source, and $\vec{\alpha}$ is the deflection angle. The apparent deflection angle $\vec{\alpha}$ is related to $\hat{\vec{\alpha}}$ by $\vec{\alpha} = (D_{LS}/D_S)\hat{\vec{\alpha}}$. The deflection angle $\vec{\alpha}$ as given by general relativity is found by integrating over the component of the potential orthogonal to the path of light:

$$\vec{\alpha} = \frac{D_{LS}}{D_S}\frac{2}{c^2}\int \vec{\nabla}_\perp \Phi \mathrm{d}\ell \tag{1.2}$$

Except for very simple lenses, (1.2) is quite difficult to calculate. With the thin screen

approximation, we let

$$\Sigma(\vec{\zeta}) = \int_0^\infty \rho(\vec{\zeta}, z)\mathrm{d}z, \tag{1.3}$$

where ρ is the three dimensional mass density of the lens, z is the direction along the line of sight through the lens, and $|\vec{\zeta}|$ is the physical distance that $\vec{\theta}$ covers in the lens plane. With this introduction, (1.2) becomes

$$\vec{\alpha} = \frac{D_{LS}}{D_S}\frac{4G}{c^2}\int \frac{(\vec{\zeta} - \vec{\zeta}')\Sigma(\vec{\zeta}')}{|\vec{\zeta} - \vec{\zeta}'|^2}\mathrm{d}^2\vec{\zeta}'. \tag{1.4}$$

Solving (1.4) is much more straightforward than solving (1.2).

One important case to consider is that of when the source is directly behind the center of the lens, i.e., $\beta = 0$. If the lens is circularly symmetric, then the image is a ring of radius θ_E, where $\alpha(\theta_E) = \theta_E$. The Einstein radius θ_E of a lens is a common measure of how strong (and therefore how massive) a lens is. In general, the deflection angle $\vec{\alpha}$ dependence on the image location $\vec{\theta}$ is nonlinear, so for a given source location $\vec{\beta}$, there is more than one possible image location $\vec{\theta}$. (One extreme example of this is in the case of $\beta = 0$; the image is smeared out into an Einstein ring rather than remaining more localized.)

Gravitational lensing also affects the apparent magnification of lensed objects. Because this information is ignored in all of the analyses presented here, we are omitting such a discussion. Finally, it should be noted that while the geometry here depends only on a set of three distances, the relation between these distances and their associated redshifts—the measurable quantities—depend on what cosmological parameters are assumed. In this paper, we assume that $h = 0.7$, $\Omega_\Lambda = 0.77$, $\Omega_M = 0.23$, and the universe is assumed to be flat (with a curvature identically equal to one).

1.3 The Need For Simulations

Algorithms for reconstructing lensing mass profiles are inherently numerical, and must make a series of approximations in order to recover a signal in the data. Furthermore, real data is not clean; the signal is diminished by noise, the atmosphere, and the telescope itself. Data reduction is often liable to add biases in what signal is actually recovered. For the results of a given method to be believable when applied to real data, they must be tested on similar data for which all of the parameters are known. This calls for image simulations that are as realistic as possible. Image simulations can also help drive the specifications for new telescopes: just how deep, how highly resolved, and how many objects do we need in order to answer the questions we want to answer?

The image simulations presented in Chapter 2 are designed to emulate the signal-decreasing effects found in a set of pointings from the Subaru Telescope. For the sake of the preliminary strong-lensing analysis presented in Chapter 3, we use two idealized simulated images with different object densities, and to approximately the same depth as the Hubble Telescope COSMOS data.

Chapter 2

Creating the Simulations

Our simulated images were created by modelling each step of how a real image comes to be. Essentially, light from background galaxies is lensed by an intervening cluster, to finally hit a detector in a telescope near or on Earth. In our case, the background wallpaper of galaxies consisted solely of galaxies from a catalog of the Cosmic Evolution Survey (COSMOS) data taken with the Advanced Camera for Surveys (ACS) on the Hubble Space Telescope (HST) [Ford et al. (2001)], as described in §2.1. Once the wallpaper in a given redshift bin was created, it was lensed by a N-body simulated 10^{15} $M_{\odot}$* 1Mpc galaxy cluster at a redshift of $z = 0.4$. The raytracing algorithm used, along with associated errors, is explained in §2.2. Finally, for these simulations to accurately reflect what is found in real data, we modelled the kind of noise and point spread function (PSF) found in the Subaru Telescope COSMOS data. For the preliminary mass reconstruction results presented in this paper, the images were left noiseless and PSF-less. However, if a study of the robustness of mass reconstruction methods on *real* data were desired, it would be simple to create an appropriate set of images, as explained in §2.3.

*More precisely, 1.078×10^{15} $M_{\odot}$; see §2.2.2.

2.1 Laying down the Wallpaper

A background "wallpaper" of galaxies is made by selecting a given number of galaxies from a catalog and placing them onto an image array. In our case, the catalog was made from the first half of the ACS COSMOS data, as explained in §2.1.1. The catalog stored the shapelets decomposition [Massey & Refregier (2005)] of each object in addition to a normal set of Source Extractor (SExtractor) parameters [Bertin & Arnouts (1996)]. For each simulated image, five sheets of background galaxies were created, corresponding to five equally spaced redshift bins between $z_{\rm lens} = 0.4$ and $z_{\rm max} = 1.765$. Each galaxy in the image was assigned to a redshift bin and placed into the image as explained in §2.1.2.

2.1.1 Cataloging the ACS COSMOS Data

The Cosmic Evolution Survey, or COSMOS, is a collaboration including the Hubble Space Telescope (HST) and many ground-based telescopes to map a two square degree patch of sky in the constellation Sextans. The galaxy catalog used for the simulations presented here was generated from the first half of the HST data, a set of 261 pointings in the i' band of the Advanced Camera for Surveys (ACS). Each pointing covers a $3\farcm83 \times 3\farcm83$ field of view consisting of 4600×4600 $0\farcs05$ pixels.

The catalog was generated using the methods of [Refregier (2003)]. Each objected was decomposed into a set of coefficients of the shapelets basis functions, Gaussian-weighted Hermite polynomials (the same basis functions as the quantum-2D harmonic oscillator). This allows for complex morphologies of the objects to be easily stored. These methods have been shown to preserve such measures of galactic morphology as clumpiness, asymmetry, and concentration [Massey et al. (2004a)].

Once all of the objects found by SExtractor in each pointing were cataloged with shapelets, the catalog had to be cleaned so that only galaxies remained in them. Most of the spurious objects were caused by the presence of bright stars in the fields. Stars are actually too small to be resolved by a telescope as anything larger than a pixel, but the point-spread function (PSF) blurs their images into adjacent pixels. The HST PSF

is due to the telescope itself, and is nonconstant over both time and the detector itself. A bright star might be unresolvable by the telescope, but cause diffraction patterns that are nonetheless sampled by the CCD's pixels. The most visible indication of this are the large vertical and horizontal spikes off of bright starts in an image caused by diffraction off of the struts holding the telescope's secondary mirror in place. For the brightest stars, these spikes are discontinuous, and SExtractor detects the different pieces as different objects. These spurious objects were removed from the catalog, as were any objects that were close enough to bright stars that their shape, magnitude, and size information were likely contaminated by the nearby saturated pixels.

Finally, each image corresponds to four dithered exposures, that is, each image corresponds to four exposures that are slightly offset from one another so as to decrease noise. Because of this, pixels near the edges of the images are much more susceptible to noise, such as gamma rays, because they correspond to only one or two exposures, instead of four. All of the objects in regions with fewer than three exposures were therefore removed from the catalog. Furthermore, images taken from adjacent regions in the sky actually overlap by a small amount. The catalog was searched for duplicate copies of objects by looking for objects with very similar right ascensions and declinations, and verifying that pairs of objects actually have similar magnitudes and sizes. One copy of each duplicate object was then removed from the catalog.

All told, there are over 625,000 galaxies in the catalogs. Because this is *many* more objects than we would want to put into one image simulation, we had the flexibility to use a large number of non-duplicated objects in any given simulation.

2.1.2 Getting Galaxies from the Catalog to the Image Array

Because the wallpaper was going to be lensed—a procedure that is sensitive to the redshift of the sources—redshifts have to be assigned to each galaxy before they were placed in the image. Unfortunately, to date, photometry has only been done for the brightest objects in the fields. The maximum magnitude in the COSMOS catalog is taken to be 29.0 (as there are a negligible number of objects dimmer than this). This

corresponds to a cutoff redshift of $z_{\text{cutoff}} = 1.765$, according to

$$z_{\text{cutoff}} = 0.722 + 0.149(\text{apparent magnitude} - 22.0). \tag{2.1}$$

As our lensing galaxy was to be placed at a redshift of $z = 0.4$, we have approximated the full range of possible redshifts with five equally sized bins between $z = 0.4$ and $z = 1.765$. Each galaxy is then assigned to a bin before placing it in the image as follows. For each galaxy, there is some corresponding magnitude, which in turn has a corresponding z_{cutoff} according to (2.1). The redshift distribution with this cutoff redshift is then given by

$$P(z) \sim z^2 e^{-z/z_{\text{cutoff}}}. \tag{2.2}$$

If z_{cutoff} is greater than 0.4, then a redshift between $z = 0.4$ and $z = 1.765$ is then selected according to this distribution, and the galaxy is assigned to the corresponding bin. A sample distribution of objects per redshift is given in Figure 2-1. [Massey et al.(2004b)]

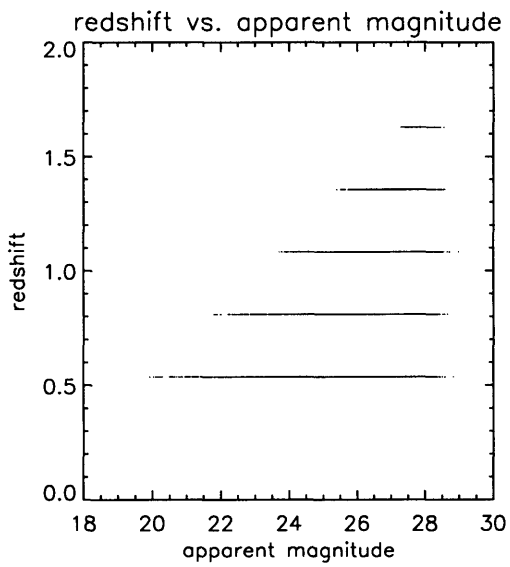

Figure 2-1: Distribution of 10,000 objects into five equally-sized redshift bins, according to apparent magnitude.

Because they must be lensed separately, the image array for each redshift is made

separately. As each galaxy for a given redshift was selected from the catalog, it was recomposed from its shapelets coefficients into a pixellated postage-stamp image. The postage-stamp was then randomly placed on the image, without the guarantee that the object would lie fully within the image border. Finally, once all of the objects are placed on the image, the image is repixellated. In the simulations presented here, this meant going from a pixel size of 0.″05 to 0.″20.

2.2 Raytracing

As mentioned in §1.2.2, there is, in general, more than one possible image location $\vec{\theta}$ for a given source position $\vec{\beta}$. This means that it is rather difficult to answer the question of where a light ray emanating from a distant source will hit a detector. On the other hand, for any one given location $\vec{\theta}$ on our detector, there is only one corresponding source location $\vec{\beta}$, as given by the lens equation (1.1). Thus, a reasonable raytracing algorithm is to solve for $\vec{\beta}$ for each image location (i.e., pixel) on the detector. We go into the details of our raytracing algorithm in §2.2.1, and in §2.2.2, we discuss the associated errors.

2.2.1 Basic Algorithm

For an image at a given position $\vec{\theta}$, we must calculate the deflection angle $\vec{\alpha}(\vec{\theta})$ as given by

$$\vec{\alpha}(\vec{\theta}) = \frac{D_{LS}}{D_S}\frac{4G}{c^2\theta}\int_0^\infty \frac{(\vec{\zeta}-\vec{\zeta}')\Sigma(\vec{\zeta}')}{|\vec{\zeta}-\vec{\zeta}'|^2}\,\mathrm{d}^2\vec{\zeta}', \tag{2.3}$$

where $\vec{\zeta}$ is the distance $\vec{\theta}$ covers in the lensing plane, $D_L\vec{\theta}$. The simple way of calculating the deflection angle $\vec{\alpha}$ is to numerically do the double integral over all of the mass elements in the field. We treat each of the pixels in the lens as a point mass at the center of the pixel. Then, for each pixel in the detector, we calculate the deflection angle, which in turn gives us a point on the source plane. The value of the pixel in which this point falls is then assigned to the pixel in the detector. (A more accurate method would be to use a weighted average of neighboring pixels, based on wherein

the pixel the point falls. But for a fine enough grid, directly assigning one pixel value is a good enough approximation.) Because this double integral must be done for each possible source position β, for an $n \times n$ array, such an algorithm has a runtime on the order of n^4. As this was found to be unacceptably slow, an alternative method was used.

The integral in (2.3) can be viewed as a convolution of the surface mass density Σ and a kernel, $1/|\vec{\zeta}' - \vec{\zeta}|$. Since both Σ and the kernel can be expressed as matrices, this calculation can be done as a simple matrix multiplication in Fourier space. By calculating the deflection $\vec{\alpha}$ in Fourier space rather than in real space, we are able to cut the runtime down to on the order of n^2.

The lensing cluster is as given an array with units of solar masses per pixel. This is the surface mass density matrix Σ. The kernel $1/|\vec{\zeta}' - \vec{\zeta}|$ can be expressed as two matrices K_x and K_y. Specifically, if d is the distance to the from a given pixel to the closest corner of the array, and d_x is the x-coordinate of this distance, then the value of K_x at that pixel is given by d_x/d^2. Letting $\tilde{\xi}$ denote the Fourier transform of ξ,

$$\tilde{\alpha_x} = \lambda \tilde{K_x} \tilde{\Sigma} \text{ and} \tag{2.4}$$

$$\tilde{\alpha_y} = \lambda \tilde{K_y} \tilde{\Sigma}. \tag{2.5}$$

Here, λ is the necessary multiplicative constant to deal with both units and the constants in front of (2.3); with G given in units of $\mathrm{m}^3/(\mathrm{kg\ s}^2)$, c in units of meters per second, $M_\odot$ in units of kilograms, all distances in units of megaparsecs, and the pixel size given in units of arcseconds, λ is

$$\lambda = \left(\frac{GM_\odot}{c^2}\right)\left(\frac{D_{LS}}{D_L D_S}\right)\left(\frac{(648000/\pi)/\text{pixel size}}{3.0856 \times 10^{22}\text{m/Mpc}}\right). \tag{2.6}$$

From (2.4,2.5), α_x and α_y are calculated by simply transforming back into real space. All possible image locations $\vec{\theta}$ must then only been looped through once, with the final source positions being given simply by $\beta_x = \theta_x - \alpha_x$ and $\beta_y = \theta_y - \alpha_y$.

2.2.2 Error Correction

The raytracing algorithm was tested using an singular isothermal sphere as a lens. While the brute-force algorithm of numerically doing the double integral was able to reliably produce the expected results, this is not strictly true for the straight Fast Fourier Transform calculation. The problem lies in that going in and out of Fourier space, periodic boundary conditions are applied. We attempted to decrease the associated errors by constructing the lens going through the FFT such that the associated α's are zero at the edges. Such an effective lens was constructed by modelling the desired lens with a known analytic one, and doing the actual Fourier transformation on the difference between the two. After the α map was created from this residual lens, the known analytic α component was added back.

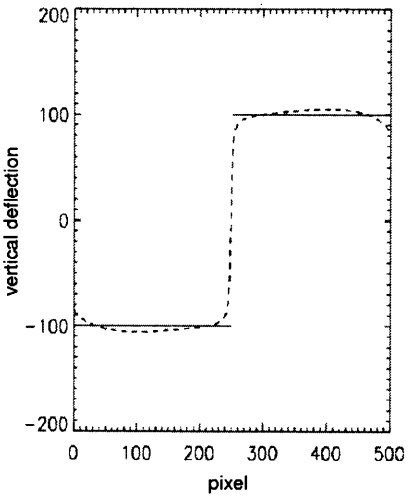

Figure 2-2: Deflection angle for isothermal sphere with $\theta_E = 100$ pixels. The solid line is the analytic solution, and the dashed line is as given by this algorithm. This is for a vertical cut along the center of a 500×500 pixel array. Deflections are only in the vertical direction.

This solution was tested on lenses as singular isothermal spheres with various Einstein radii. For an $n \times n$ pixel array, the isothermal sphere was modelled as a lens with a linear radial mass profile (i.e., conical) that had the same deflection $\vec{\alpha}$ at a radius of $(n/2)\sqrt{\sqrt{2}}$. The effective lens, the isothermal sphere minus the conical lens, was then put through the Fourier transform. When the final deflection angle

was calculated, the known analytic component from the conical lens was added back in. As shown in Figure 2-2, we found this method of α-matching to work reasonably well. As expected, most of the problems are at the edges still, but we believe that for the center of the image, the locations of the images are believable, and any remaining errors are on the order of unity.

Because the cluster used in the simulations discussed in Chapter 3 had to be placed in a slightly larger box in order to facilitate α-matching at the edges, the *total* mass of the lens was the mass of the cluster plus the mass of these extra wings, for a total mass of $1.078 \times 10^{15} M_{\odot}$. The α-matching was done by approximating the cluster as an isothermal sphere.

2.3 Making It Real: PSF and Noise

The image simulations used for the preliminary analysis presented in Chapter 3 are idealized; they are free of the noise and distortions associated with data taken by a real telescope. However, if the potential of mass reconstruction techniques to work on real data is to be truly tested, the image simulations must be as realistic as possible. Furthermore, if we want to know to what specifications future telescopes are to be built, it would be nice to know the upper limits on various noise and PSF parameters such that the data from such telescopes will still be acceptable for doing the analyses that we would like to do. In order to make the image simulations as realistic as possible, a specific set of real data to emulate is needed. We chose to emulate a set of pointings taken with the Subaru Prime Focus Camera (Suprime Cam) as part of COSMOS[Komiyama et al. (2003)]. Because HST is potentially no longer being serviced and it will be several more years before another suitable space-based telescope is launched, most gravitational lensing studies in the near future will be done with ground-based data from telescopes like Subaru. It is also an added bonus that the patch of sky covered by the HST and Subaru data is the same; because the objects detected by Subaru are a subset of those detected by HST, we should theoretically be able to approximately reproduce the Subaru data by simply degrading the HST

data.

The point spread function (PSF) describes how a single point of light is blurred out into adjacent pixels. While the PSF is scientifically uninteresting—it is due to telescope irregularities and turbulence in the Earth's atmosphere—it is important to model well because a typical PSF has an ellipticity on the order of the signal found in the weak lensing limit. Our goal was to model a reasonable, realistic PSF—not to determine exactly the Subaru COSMOS PSF, which varies across the CCD and over time. We therefore could look at only the nicely bright, but unsaturated, stars for all ten of the Subaru pointings. Because the PSF varies across the CCD, the image field was divided up into a grid of 1.′75 squares as shown in Figure 2-3. The shapelets coefficients for all of the stars falling into each square were averaged and cataloged. Stars were thrown out if their shapelets decomposition was flagged as "bad" by the shapelets software. Every decomposition in shapelets is given a χ^2 based on a comparison between the original object and a reconstructed one; stars were also thrown out of the samples if their χ^2 was large. A catalog of 240 PSFs was then made from which a PSF could easily be selected in the image creation process; only one PSF is applied to each image. Because a real PSF does not come in to play until well *after* background objects are lensed, the image array is not convolved with a chosen PSF until after all of the objects have been placed on the array for a given redshift and the image has been run through the raytracing program. A typical PSF had a full-width half-max (fwhm) of 3.03 pixels and a mean ellipticity of 1.4%. (A circle is said to have an ellipticity of 0%, while a line has an ellipticity of 100%.)

This approach to modelling the PSF treats the PSF as constant over time and space, which is not realistic. However, it is still reasonable because these images had an exposure time of forty minutes, during which the PSF did in fact change. Also, most of the current methods for PSF correction assume that the PSF is constant over small patches of the detector. This method for modelling the PSF is also more realistic than most because by using shapelets to model the PSF, it is allowed to have a more complex shape than just a certain ellipticity and size would dictate.

As with the PSF, the noise parameters yield both a typical level of noise and are

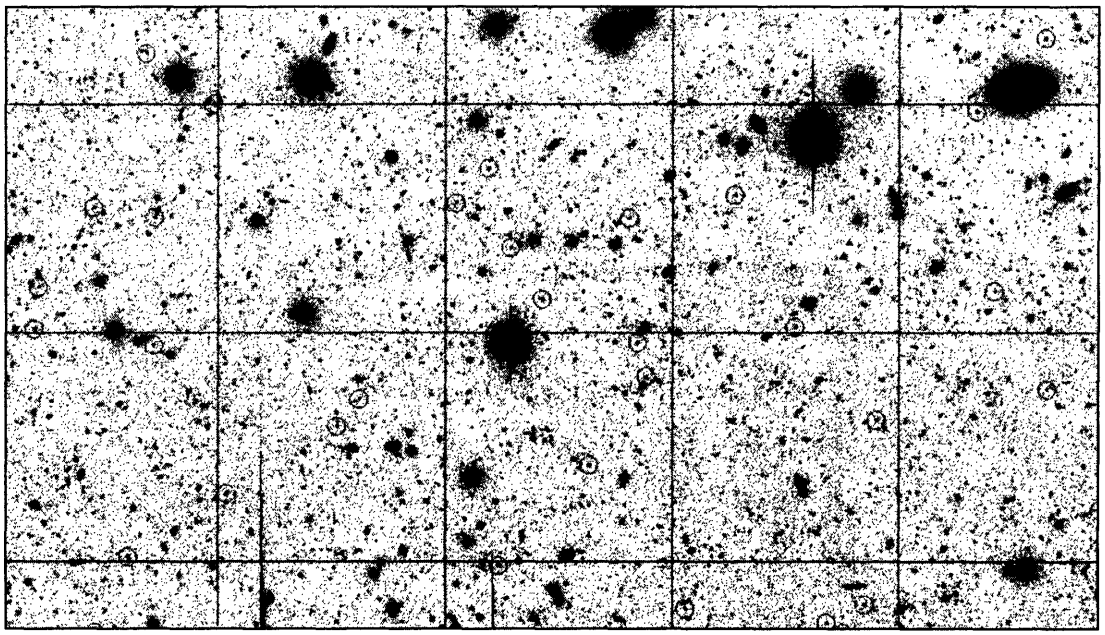

Figure 2-3: Example image with stars used to model the PSF circled. Each pointing was divided up into squares, as shown here; the shapelets catalog information for each selected star per square was averaged in order to generate a sample PSF for that region.

physically motivated. The exposure time was set to be the same as for the total exposure time per pointing for the Subaru data, which was forty minutes (2.4ks). The gain associated with the Suprime Cam CCDs is 2.6 ADU/e^-.[Komiyama et al. (2003)] The shot noise parameter—the root mean squared (rms) of the noise proportional to the photon count in each pixel—is set to be the square root of the ratio of the gain to the exposure time. The background noise parameter, which corresponds to the rms of the sky background level, is proportional to $\sqrt{2000 \times \text{gain}/(\text{exposure time})}$. The factor of 2000 corresponds to the original background level of the Subaru pointings in ADU.

To add noise to the image, the array is first renormalized to correspond with the exposure time of the Subaru pointings, rather than the original catalog. Next, the shot noise is added to the image, where the noise per pixel is calculated to be the product of the square root of the value of that pixel and a random number according to a gaussian distribution with a zero mean and a standard deviation of the shot noise

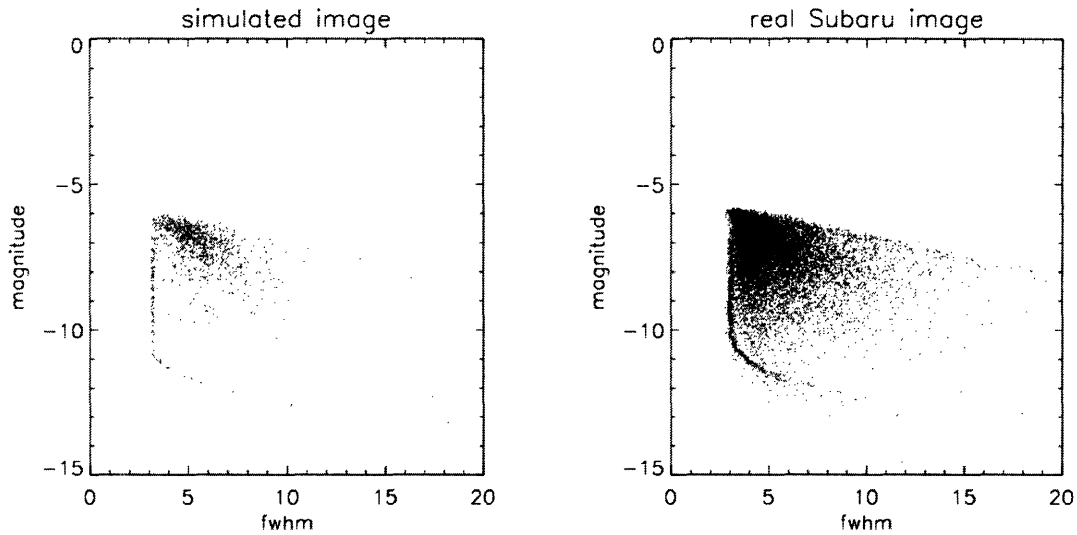

Figure 2-4: Magnitude versus full-width half-max for an unlensed simulated image, on the left, and a real image, on the right. Each data point in these plots corresponds to one object in the image.

parameter. The background noise is incorporated into the image by first calculating a noise array—unlike the shot noise, the background noise does not depend on the number of photons hitting the CCD. Each entry in the noise array is first given a random value according to a gaussian distribution around the background noise parameter. The noise array is then smoothed by a gaussian with a fwhm of 3.5 pixels. As this process is to simulate the "clumpiness" seen in the background noise, the kernel size of 3.5 pixels was chosen because it is approximately equal to the average seeing. The noise array renormalized to correspond to the correct exposure time, and then added to the image. This process yields a background noise that is much more uniform across an entire simulated image than is found in a real images. Locally, however, it is quite characteristic of what is seen in the Subaru data.

These noise parameters were found to yield a very realistic level of noise. Figure 2-4 shows plot of magnitude versus fwhm for an unlensed simulated image and a real Subaru image. Even though there are many objects from the ACS COSMOS catalog that are smaller than seen in the Subaru data, these objects are not detected by SExtractor in the simulated image because the noise effectively drowns them out. The distinct vertical line around a fwhm of 3.5 pixels in the two plots corresponds to

the stars in the images. Note that while Subaru might be able to resolve the smaller galaxies in the ACS catalog, the seeing makes it very difficult to actually discriminate between faint stars, small faint galaxies, and noise. (For the analysis presented in the next chapter, the simulated images contained no noise, no PSF, and no stars—just lensed background objects.)

Because the different sources of noise are parameterized separately, it is possible to vary them independently of one another. Likewise, one can incorporate any known PSF, such as one modelled from a specific telescope design. This freedom allows us the potential to determine to what specifications a telescope must be designed to be able to gather data that will be able to be reasonably analyzed.

Chapter 3

Mass Reconstruction

When reconstructing a mass distribution using information from gravitational lensing in both the strong and weak limits, the driving question is whether or not a certain distribution would lead to the distortions seen in the data. In the regime of strong lensing, just the multiply-imaged objects and large arcs are considered. Because this means focussing on just the more massive portions of the lens, a strong lensing attack is expected to under-estimate the total mass in the lensing cluster. On the other hand, it is theoretically possible to detect substructure—that is, deviations from the central peak—in the lensing cluster by analyzing the arcs and multiply-imaged galaxies.

Here we present a preliminary strong lensing analysis of the image simulations presented in Chapter 2. These images are idealized and clean; they do not include any of the noise or PSFs discussed in §2.3. In §3.1, we briefly describe how the Strong Lensing Analysis Package (SLAP) analyzes strongly lensed objects to give a mass distribution. In §3.2, we compare the results of this procedure to the actual lensing cluster. The algorithm presented here is a recent improvement on that presented in [Diego et al. (2005)], and the actual analysis was done by J. M. Diego.* The total detectable mass was about 20% less than the actual mass, and most of the substructure was unresolvable.

For the sake of clarity in the following discussion, we will use the term "pointing" to refer to a picture array from a telescope or the image simulations discussed in

*http://darwin.cfa.harvard.edu/SLAP/

Chapter 2. The term "source" will refer to the background galaxies *before* they are lensed; following the notation introduced in Chapter 1, the source position is given by $\vec{\beta}$. Finally, "image" will refer to one of the pixels in one of the objects in a pointing that is being studied.

3.1 From Arcs to a Mass Distribution

The first step in determining a mass structure from the strong lensing information is to actually gather the strong lensing information from the image, i.e., to identify any sufficiently large "arcs" and multiply-imaged objects. For a given pointing, it is known which images correspond to which sources, and therefore which sources are multiply imaged. Using this information, a set of suitable arcs and other multiply-imaged objects are selected to be used in the analysis. Figure 3-1 shows such a selection for the two images used in this study. Note that in the center of the image, radially stretched galaxies are visible. A certain background level of noise is assumed, and any pixel in the object with a value above that noise is determined to be part of that object. There are a total of N_{pix} pixels covered by these N_{obj} images. (To speed up the algorithm, a representative sample of pixels can be taken.) This particular algorithm uses solely the *positions* of the images, completely ignoring any magnification effects.

Consider the lens equation, (1.1). For the ith image position, this can be rewritten in matrix form as

$$\beta_i = \theta_i - \Upsilon_{i\mu} M_\mu, \tag{3.1}$$

where the deflection α_i has been rewritten as

$$\begin{pmatrix} \alpha_i^x \\ \alpha_i^y \end{pmatrix} = \begin{pmatrix} \Upsilon_{i\mu}^x \\ \Upsilon_{i\mu}^y \end{pmatrix} M_\mu, \tag{3.2}$$

with the information on how the ith deflection angle is affected by the mass element μ being stored in $\Upsilon^{x,y}$. The mass is taken to be divided up into a grid of N_{cells} cells, as explained below. Each mass element is in a square cell and taken to have a gaussian

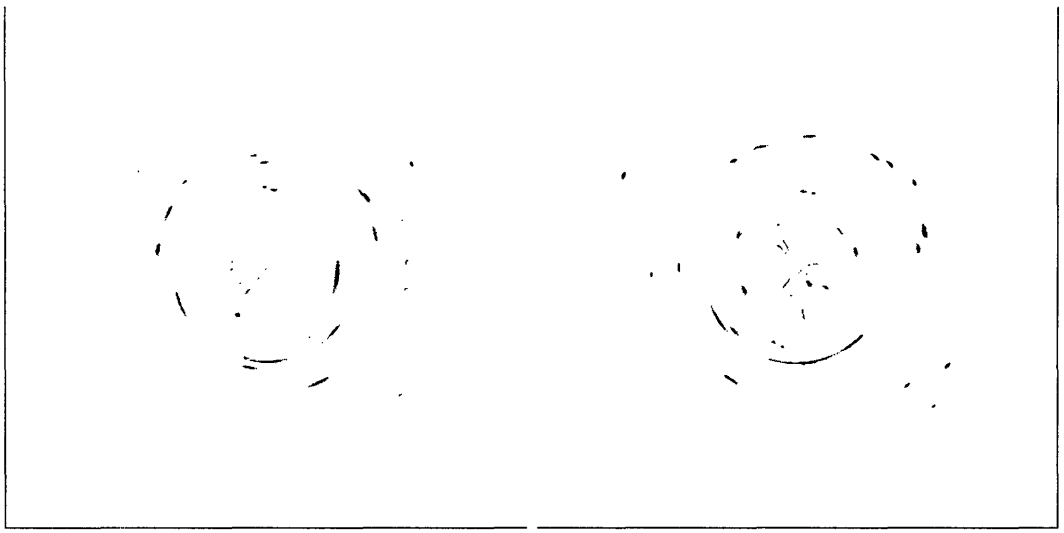

Figure 3-1: Samples of arcs and multiply-imaged sources for strong lensing analysis. Left: 12 sources & 27 objects. Right: 17 sources & 38 objects. The left pointing initially had 690 objects; the right, 1217.

distribution with a standard deviation of σ = width/0.55; the 0.55 is so that the mass distribution can have as smooth a profile as possible. Υ^x and Υ^y are therefore a $N_{obj} \times N_{cells}$ matrices. Because the size and locations of the mass cells are stored in Υ^x and Υ^y, once the masses M_μ are solved for, the surface mass density is known. By assuming that the sources are point-like even though their images are compact, the number of unknowns is reduced, and (3.1) can be simplified to

$$\begin{pmatrix} \theta_x \\ \theta_y \end{pmatrix} = \begin{pmatrix} \Gamma^x \\ \Gamma^y \end{pmatrix} X, \tag{3.3}$$

where all of the unknowns are stored in X, and all of the other information—mass and source locations—is stored in $\Gamma^{x,y}$. There are $N_{cells} + 2N_{source}$ unknowns; the 2 accounts for both the x and the y positions of each source. The $\Gamma^{x,y}$ matrices are exactly the same as $\Upsilon^{x,y}$, but with $2N_{source}$ additional columns. Explicitly, with $\hat{\xi}$

denoting a matrix and $\vec{\xi}$ denoting a vector, (3.3) is

$$\begin{pmatrix} \vec{\theta_x} \\ \vec{\theta_y} \end{pmatrix} = \begin{pmatrix} \hat{\Upsilon}_x & \hat{1} & \hat{0} \\ \hat{\Upsilon}_y & \hat{0} & \hat{1} \end{pmatrix} \begin{pmatrix} \vec{M} \\ \vec{\beta_o^x} \\ \vec{\beta_o^y} \end{pmatrix}. \tag{3.4}$$

The $\hat{1}$ matrices in (3.4) keep track of which image pixels correspond to which sources, while the 0's in are just to keep track of the coordinates. Thus solving for X is equivalent to solving for the mass density and source locations.

The solution to (3.3) is the same as the minimum of

$$R^2 = (\theta - \Gamma X)^T (\theta - \Gamma X), \tag{3.5}$$

which can be solved using any of the standard minimization algorithms for quadratic functions. Here, the bi-conjugate gradient is used [Press et al. (1997)]. One of the problems with minimizing a quadratic equation, however, is that the minimum might be less than zero, which would correspond to negative mass. Negative mass is somewhat unphysical, so such a solution is less than ideal. A recent improvement to this algorithm has been to constrain the solutions to (3.5) to be positive. Finding the absolute minimum is also equivalent to assuming that the sources are all point sources—which they are definitely not. Instead, the sources are assumed to be 10kpc in extent, and the minimization stops when it reaches a solution that is consistent with this assumption. (While the choice of 10kpc is arbitrary, the minima found do not change appreciably with choices within a range of 5–20kpc.) Because the solution depends on the seed with which the minimization is started, the minimum is found with 1000 different seeds, and the results from each of these minimizations is averaged to find the "real" answer. This minimization is achieved by using the so-called quadratic programming algorithms, which can find a minimum of (3.5) under the constraint that all of the masses must be positive.

To find the mass distribution, the field of view was initially divided up into a coarse grid of equally sized masses, with the total mass equal to some seed. (3.5) is

then interatively minimized. At each step, the more massive regions from the results of the previous step are divided up into a finer grid so as to increase resolution in those areas. This method usually converges after five or six iterations; such an example is shown in Figure 3-2.

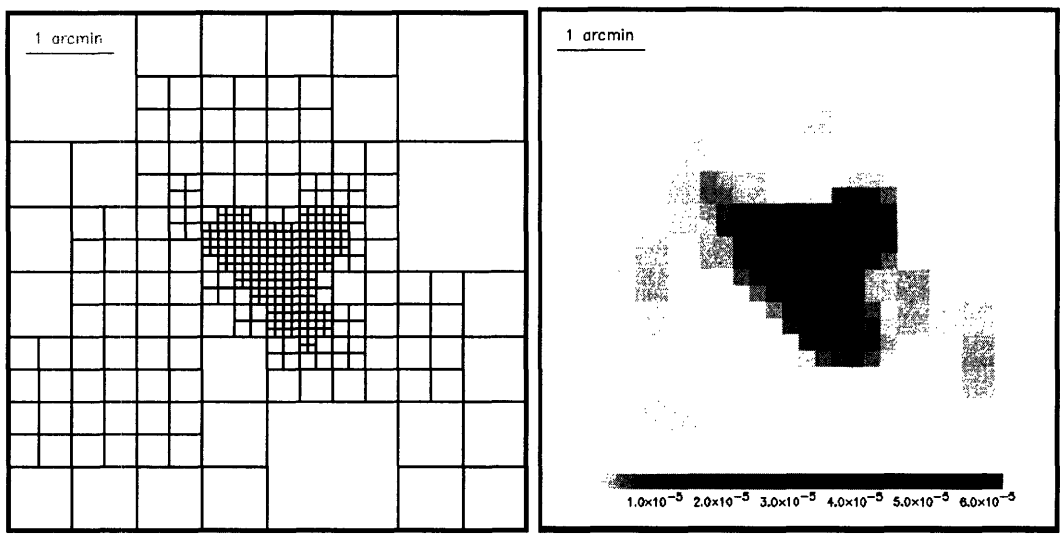

Figure 3-2: Example of non-uniform grids for optimizing surface mass density.

3.2 Comparison to Original Cluster

We found this procedure to be decent at reconstructing the mass profile of our lensing galaxy. As expected, the total retrieved mass was less than the input mass by roughly 20%. Furthermore, while this procedure did succeed in finding some substructure, it was unable to highly resolve said structures. There were also clumps in the reconstructed mass that do not directly correspond to peaks in the initial cluster.

Two pointings with different densities of objects were analyzed: one with a total of 690 objects identified by SExtractor, and the second with 1217. (The input number of galaxies was 1000 and 2000 respectively, but the lensing causes objects to move outside the field of view.) The analysis used twelve sources and twenty-seven arcs in the first image, and seventeen sources and thirty-eight arcs in the second (see Figure 3-1). The $3'.43$ fields of view were initially divided up into 256 squares, and (3.5) was

iteratively minimized five times. Using the pointing with fewer arcs, a total mass of 7.64×10^{14} solar masses was recovered, while the pointing with more objects detected slightly more at 8.39×10^{14} solar masses. (The original mass was 1.078×10^{15} $M_{\odot}$.)

As seen in Figure 3-3, the overall radial surface density for the two were fairly similar, although it could be argued that the pointing with more sources was able to detect more of the interior mass. Note that the both reconstructed profiles begin to agree with the original profile at around fifty arcseconds, which approximately corresponds with the locations of the outermost arcs in both pointings. The true steepness of the *inner* profile, however, was unable to be detected from either pointing. This is because the data does not actually represent the very center of the cluster, rendering the algorithm insensitive to this region. On the other hand, there are many more pixels in the larger, outermost arcs; these data points therefore dominated the algorithm, making the results more sensitive to the total mass than to the intrinsic profile. Finally, the mass profile was treated as a superposition of smaller gaussian profiles; this means that while the original profile goes like r^{-1} at the center, the reconstructed profile will go like r^0, i.e., it will be flat. All told, this raises the question of whether or not the inner surface mass profiles of clusters are actually steeper than we believe them to be and we are simply unable to accurately measure them.

The final reconstructed mass and residual for the pointing with seventeen sources are shown alongside the original cluster in Figure 3-4. Note that the central peak in the original cluster is somewhat elliptical; it is elongated in the "vertical" direction. While the profiles in Figure 3-3 indicate that the reconstruction was unable to detect the expected amount of mass interior to the outermost images, the residual map indicates that the reconstruction did in fact somewhat overestimate the mass in the regions outside of the central peak and within the radius of the outermost arcs ($50''$), but not by enough to account for all of the actual mass within this radius. Furthermore, the regions over slight overestimate are approximately along the long axis the central elliptical peak, rather than on the sides. Finally, the residual map indicates that outside of the critical radius of fifty arcseconds, the reconstruction did

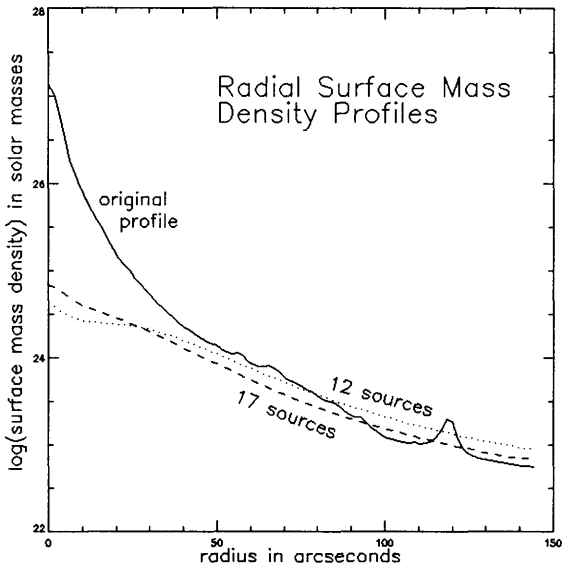

Figure 3-3: Surface mass density as a function of a radius.

a fairly decent job at representing the underlying profile, aside from not being able to resolve the peakiness of the off-center clumps.

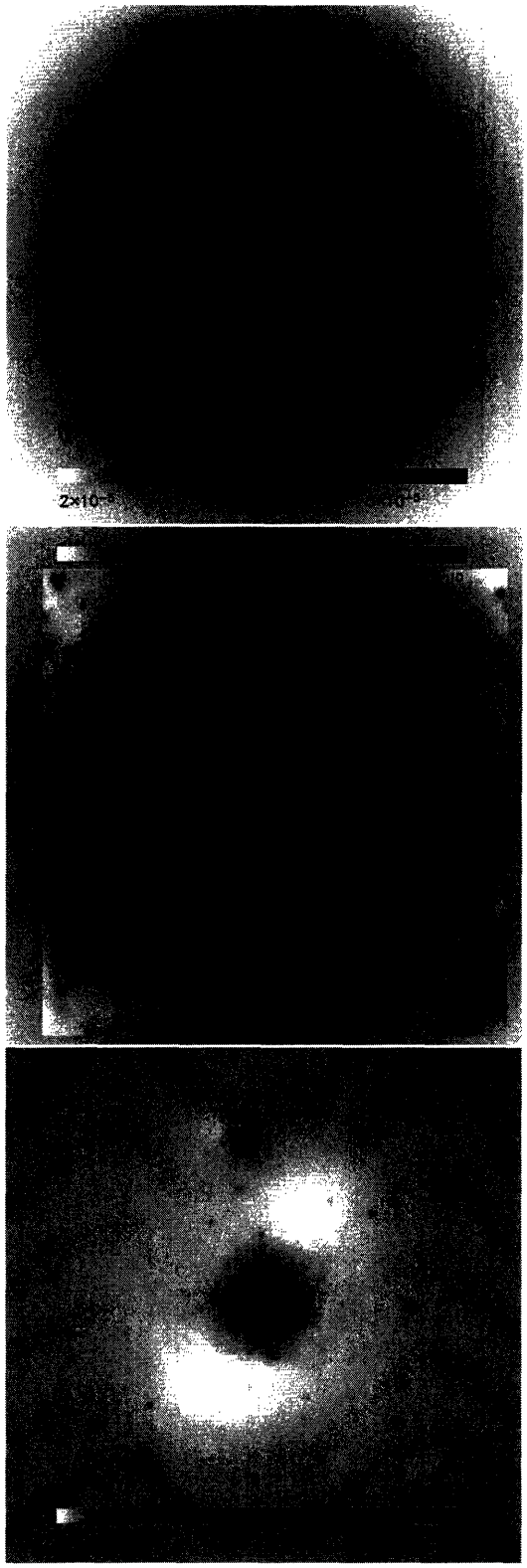

Figure 3-4: Top: Reconstructed cluster from pointing with 17 sources. Middle: Original cluster. Bottom: Residual (original minus reconstructed). All pointings are $3'.42 \times 3'.43$. Note from the residual that while the reconstruction failed to reproduce the central peak, it did overestimate the mass found above and below the center of the pointing.

Chapter 4

Discussion

We find the simulations presented here to have the potential to help answer the questions of how much can be learned about the mass distribution within galaxy clusters via gravitational lensing. Questions of how these simulations could be improved are addressed in §4.1. As it is the dark matter profiles in the innermost regions of clusters that most interests us, and these are the regions in which the analysis presented in Chapter 3 failed, we suggest in §4.2 to include in the analysis the objects in the weak lensing limit.

4.1 Making the Simulations More Realistic

If these simulations are to be used to test the robustness and accuracy of mass reconstruction techniques' abilities to glean information from real data, then they must be as realistic as possible. In this section, we first review how realistic and not realistic the current simulations are in §4.1.1, and in §4.1.2 we offer some solutions for addressing the less realistic aspects.

4.1.1 Reality Check

The Good

Both the galaxy cataloging described in §2.1.1 and the Subaru data emulation described in §2.3 are quite realistic. Because the objects in these simulations have complex structures, they have the potential to be quite useful in morphology studies. Furthermore, because real data is sullied by noise and a PSF, a real data analysis pipeline must take into account both of these factors. For instance, noise is likely to reduce the number of detectable radial objects that are visible in Figure 3-1. A PSF must be accurately corrected for before any useful information is gathered from a weak lensing study. This image simulation pipeline could easily generate a set of lensed images that could test the ability of these reconstruction techniques to deal with noise and nasty PSFs.

The Bad

The photometric analysis for the data used to generate the galaxy catalogs for these simulations has not yet been finished. This means that we do not actually know the redshifts for most of the objects. Furthermore, the ACS COSMOS data is not very deep; if we want to try to answer the question of how much better we can do with a deeper survey, then the catalogs as they are are simply not good enough.

The lensing cluster used here is also not ideal. It is at an evolutionary state of $z = 0$, which means it does not look like it would actually look were it at $z = 0.4$. We also did not have a particular mass associated with the cluster; the choice of 10^{15} solar masses was arbitrary. Finally, in a real image showing background galaxies being lensed by a foreground cluster, galaxies in the cluster itself will be visible. That is to say, light from the cluster itself is a source of contamination which must be accounted for in a real data reduction pipeline. Noise from the cluster itself will also greatly diminish the signal from the central radially stretched objects, as well as other dim objects.

The Ugly

Finally, the raytracing program has unavoidable errors due to boundary conditions. Consider, for example, the right image in Figure 3-1. Is the not quite circular distribution of images in the upper righthand corner because of substructure in the lens, or is it a side effect of the raytracing program? In general, by examining a uniformly distributed set of background sources, it is painfully easy to see biases in the vertical, horizontal, and diagonal directions for even the lens used here, for which α was matched exactly at the edges. While we believe the errors introduced by this method to be acceptable, they still present a very real contamination of the data in both the strong and weak lensing limits.

4.1.2 Some Potential Solutions

Some of these problems have obvious solutions; others are more subtle. Obviously, better cluster simulations should be used—specifically, ones with specific associated masses and redshifts. For a more complete study, it would be ideal to use the same cluster at different evolutionary states. Furthermore, if the cluster itself is to be included in the image, then there must be some model of what mass in the cluster corresponds to light in the band in question (e.g., i'), and at what magnitude. This could mean incorporating a model of how baryonic matter interacts, which is not only rather complicated, but also not well known. Such models would be unnecessary for answering the question of how much we can learn via gravitational lensing—there just needs to be *some* correlation that we can then try to recover.

Obviously, once photometry is done on the COSMOS data, that information should be incorporated into the catalogs. The question of how to alter the catalog to simulate deeper data, however, is subtler. Galaxies at higher redshifts have different magnitudes (both apparent and absolute), different sizes (both angular and comoving), and different morphologies than the same galaxies would have at a later time. All of these factors would have to be taken into account in altering and selecting from the catalogs to simulate higher redshift data.

The trickiest problem here, however, is that of a raytracing algorithm that is both accurate and fast. The problems here arose from the fact that the convolution was done in Fourier space, which imposed periodic boundary conditions. One clear way to circumvent this aspect would be to do the convolution in some space that does not impose such boundary conditions, i.e., one that uses *localized* functions as a basis, rather than periodic ones. One such space is shapelets space, which is already equipped to do such convolutions; for instance, this is exactly how galaxies are convolved with a PSF in a shapelets-generated simulation. The main precaution here would be to use a sufficiently large number of coefficients such that the lensing cluster could be reasonably decomposed into shapelets and not lose vital information such as spiky peaks or off-center clumps. While this would basically require writing the lens equation in terms of shapelets, we believe that it would be possible to find $\vec{\alpha}(\vec{\theta})$ using shapelets.

4.2 Renovating the Mass

It is clear that while examining the strong lensing information in an image has the potential to help us learn about cluster structure, it does not give the whole picture. The analysis presented in Chapter 3 does not use all of the information available. It completely ignores all image magnitudes, even though such information is commonly used in strong lensing studies (such as the lensing of quasars by galaxies). A strong lensing approach also greatly limits the number of sources available for study; because background sources are only multiply imaged and severely distorted relatively close to a sufficiently large surface mass density in the lens, strongly lensed images are confined to these regions. Such sources correspond to very limited central regions of the cluster. To obtain information about the overall mass distribution of the cluster—and to detect *all* of the cluster's mass—objects further from the lens must be considered. In this weak lensing limit, the shapes background objects are only slightly distorted. By approximating the lens as an analytic profile, such as a singular isothermal sphere or an NFW profile, one is able to both locate the center of the profile

as well as estimate the total mass in the cluster. This mass is known as the aperture mass because such information is found by optimizing the location and size of the effective aperture of the lens. The aperture mass of a lens is given by

$$M_{ap} = \Sigma \gamma_t \mathcal{W}(r), \tag{4.1}$$

where γ_t is the change in an object's ellipticity in the direction tangential to a circle centered at the aperture center and $\mathcal{W}(r)$ is some weighting function specific to the modeling mass profile. As M_{ap} is a function of the position, size, and profile of the aperture, on optimal M_{ap}—one for which the signal-to-noise ratio is greatest—can be found by varying these parameters [Schneider (1996)]. By combining such an expansive profile with the structure found from examining the strongly lensed images, a more holistic and accurate depiction of the cluster might be able to be achieved.

Bibliography

[Binney & Tremaine] Binney J. & Tremaine S., 1987. *Galactic Dynamics.* Princeton University Press.

[Bertin & Arnouts (1996)] Bertin E. & Arnouts S., 1996, A&AS, 117, 393B.

[de Blok & Bosma (2002)] de Blok W. J. G. & Bosma A. 2002. A&A, 385, 816.

[de Blok et al. (2001)] de Blok W. J. G., McGaugh S. S., Bosma A., Rubin V. C. 2001. ApJ, 552, L23.

[Diego et al. (2005)] Diego J. M., Protopapas P., Sandvik H. B., Tegmark M., 2005, MNRAS in press, preprint astro-ph/0408418

[Ford et al. (2001)] Ford H. C. & Advanced Camera for Surveys Science Team 2001, Bulletin of the American Astronomical Society, 33, 1316.

[Hogg (1999)] Hogg D., astro-ph/9905116

[Komiyama et al. (2003)] Komiyama Y., et al., 2003, SPIE, 4841, 152.

[Massey et al. (2004a)] Massey R., Refregier A., Conselice C. & Bacon D. 2004, MNRAS, 348, 214

[Massey et al.(2004b)] Massey, R., Rhodes, J., Refregier, A., Albert, J., Bacon, D., Bernstein, G., Ellis, R., Jain, B., McKay, T., Perlmutter, S., Taylor, A. 2004, AJ, 127, 3089M.

[Massey & Refregier (2005)] Massey R. & Refregier A. 2005, MNRAS submitted, preprint astro-ph/0408445

[Natajaran et al. (2002)] Natajaran P., Kneib J. P., Smail I., 2002, ApJ, 580, L11

[Navarro, Frenk, & White (1997)] Navarro J., Frenk C. S., White S. D. M., 1997, ApJ 490, 493

[Press et al. (1997)] Press W. H., Teukolsky S. A., Vetterling W. T., Flannery B. P., 1997, *Numerical Recipes in Fortran 77.* Cambridge University Press.

[Refregier (2003)] Refregier A. 2003, MNRAS, 338, 35

[Roediger et al. (2005)] Roediger E. & Hensler G., 2005, A&A, 4333, 875R.

[Sand et al.(2004)] Sand D. J., Treu T., Smith G. P., & Ellis R. S. 2004, ApJ, 604, 88

[Schneider (1996)] Schneider P., 1996, MNRAS, 283, 837.

[Simon et al. (2003)] Simon J. D., Bolatto A. D., Leroy A., Blitz L. 2003. ApJ, 596, 957.

[Spergel et al.(2003)] Spergel, D. N., et al. 2003, ApJS, 148, 175 .

[Swaters et al. (2003)] Swaters R. A.,Madore B. F., van den Bosch F. C., Balcells M. 2003. ApJ, 583, 732.